PTEP

Pulsed neutron-beam focusing by modulating a permanent-magnet sextupole lens

Masako Yamada[1,2,4,*], Yoshihisa Iwashita[2], Masahiro Ichikawa[1], Yasuhiro Fuwa[1], Hiromu Tongu[2], Hirohiko M. Shimizu[3,8], Kenji Mishima[3,9], Norifumi L. Yamada[3], Katsuya Hirota[4,8], Yoshie Otake[4], Yoshichika Seki[4], Yutaka Yamagata[4], Masahiro Hino[5], Masaaki Kitaguchi[5,8], Ulf Garbe[6], Shane J. Kennedy[6], Wai Tung Lee[6], Ken H. Andersen[7,10], Bruno Guerard[7], Giuliana Manzin[7], and Peter Geltenbort[7]

[1]*Department of Physics, Kyoto University, Kyoto 606-8502, Japan*
[2]*Institute for Chemical Research, Kyoto University, Uji, Kyoto 611-0011, Japan*
[3]*High Energy Accelerator Research Organization, Tsukuba, Ibaraki 305-0801, Japan*
[4]*RIKEN Center for Advanced Photonics, Wako, Saitama 351-0198, Japan*
[5]*Kyoto University Research Reactor Institute, Kumatori, Osaka 590-0494, Japan*
[6]*Bragg Institute, ANSTO, PMB#1, Lucas Heights, NSW 2234, Australia*
[7]*Institut Laue-Langevin, 71 avenue des Martyrs, 38000 Grenoble, France*
[8]*Present address: Department of Physics, Nagoya University, Nagoya 464-8602, Japan*
[9]*Present address: International Center for Elementary Particle Physics, University of Tokyo, Bunkyo, Tokyo 113-0033, Japan*
[10]*Present address: European Spallation Source ESS AB, Box 176, 22100 Lund, Sweden*
*E-mail: masako.yamada@psi.ch

....
We have developed a compact permanent-magnet sextupole lens for neutrons that can focus a pulsed beam with a wide wavelength range—the maximum wavelength being more than double the minimum—while sufficiently suppressing the effect of chromatic aberration. The bore diameter is ø15 mm. Three units of a double-ring sextupole with a length of 66 mm are cascaded, resulting in a total length of 198 mm. The dynamic modulation range of the unit-averaged field gradient is 1.06×10^4–5.86×10^4 Tm^{-2}. Permanent magnets and newly developed torque-canceling elements make the device compact, its production costs low, and its operation simpler than that of other magnetic lenses. The efficacy of this lens was verified using very cold neutrons. The diameter of the focused beam spots over the wavelength range of 27–55 Å was the same as that of the source aperture (2 mm diameter) when the magnification of the optical arrangement was unity. The total beam flux over this wavelength range was enhanced by a factor of 43. The focusing distance from the source to the detector was 1.84 m. In addition, in a demonstration of neutron image magnification, the image of a sample mask magnified by a factor of 4.1 was observed when the magnification of the optical arrangement was 5.0.
....
Subject Index   G12

1. Introduction

Neutron beams have contributed to investigation of the static and dynamic structures of substances because of their unique features based on the interaction with the nucleus and its magnetic dipole moment. However, the neutron-beam flux is not as high as that of X-rays. Neutron optical devices can be effectively used to increase neutron utilization efficiency and measurement resolution in some instruments.

A lens can increase the beam flux at the sample position in scattering experiments by focusing and increase the spatial resolution in imaging experiments by magnifying the transported image. Besides, small-angle neutron scattering (SANS) is a suitable application for a lens because the accessible q-region can be extended to lower values with enhanced beam flux. Many SANS instruments that are under user program operation equip focusing devices for this purpose. Neutron lenses can be classified into four groups based on the following effects of de Broglie wave behavior: Bragg diffraction [1], refraction [2,3], reflection [4–6], and magnetic refraction [7–9]. Refractive lenses are advantageous in that it requires less stringent precision in beam alignment and can magnify or reduce a transported image easily. One of refractive lenses, a biconcave material lens with a large aperture, have been installed into such reactor-based monochromatic SANS and reflectometer instruments as SANS-J-II at JAEA [10], NG7 SANS at NIST [3,11], and QUOKKA at ANSTO [12].

On the other hand, neutrons are free from interaction with the material in a magnetic refractive lens, while absorption in a refractive lens and diffuse scattering in a reflective lens deteriorate the beam quality. This results in measurements with a good signal-to-noise ratio (S/N), which favors scattering experiments such as SANS. A magnetic refractive lens can focus only neutrons with spin parallel to the magnetic field. On the other hand, neutrons with antiparallel spins diverge, which may cause background noise in a detector. By selecting neutrons whose spins are parallel to the magnetic field upstream of the magnet, all the selected neutrons are focused. This polarizing process reduces the beam flux by half, which is not a disadvantage in an experiment that requires a polarized beam. In fact, SANS-J-II has also equipped a magnetic refractive lens for another focusing geometry with a polarized monochromatic beam [10]. The maximum beam divergence that magnetic lenses can handle, however, is smaller than that of focusing mirrors for the same neutron energy. Therefore, the energy range of neutrons that can be focused by magnetic lenses is comparable to or lower than that of cold neutrons.

Accelerator-driven neutron sources have been constructed and are under construction, and have become more popular than before. Energy spectroscopy using a pulsed neutron beam with the time-of-flight (TOF) method possesses very high neutron utilization efficiency. Therefore, optical devices and detectors that consist of a TOF-type neutron instrument need to handle pulsed beams with a wide wavelength range. However, only a few lenses with this functionality have been developed: (i) an ellipsoidal or paraboloidal mirror [5], (ii) a sextupole electromagnet (EM) [13], and (iii) a sextupole permanent magnet (PM) with a variable effective length and spin flippers [14–16]. To add to these lenses, we have developed (iv) a lens based on a permanent sextupole magnet with the capability of continuous field modulation via a rotating double-ring structure, called the rotating/modulating permanent-magnet sextupole (mod-PMSx) [17–19].

An ellipsoidal mirror (i) is more suitable for use as a neutron guide than a magnetic lens since it can handle a wider wavelength range. Furthermore, its focusing distance is shorter than that of a magnetic lens at the same wavelength and it can thus focus thermal neutrons. It has no moving or electrical parts and therefore does not require frequent maintenance. A toroidal double-focusing mirror is used in a running focusing SANS and reflectometer, KWS-3 at Jülich, with a monochromatic beam [20,21]. Furthermore, a TOF focusing SANS with axisymmetric Wolter mirrors has been tested [22]. These focusing mirrors, however, do not have both wide wavelength ranges, because they only have mono-layer coatings. It is still difficult to manufacture the quadric surface of an ellipsoid or paraboloid and achieve sufficiently low diffuse scattering from multilayers at a reasonable

cost and in a short manufacturing time. Furthermore, supermirror coatings on such quadric surfaces that enhance the solid angle of a reflective lens have not yet become practical. A focusing SANS using supermirror-coated ellipsoidal mirrors that can provide a beam with a wider wavelength range and beam divergence is a future challenge. Alternatively, sequential focusing in the horizontal- and vertical-beam planes using crossed 1D elliptical Kirkpatrick–Baez supermirrors is more practical and has succeeded in microfocusing to a spot size of 90 μm [23].

On the other hand, magnetic lenses can also focus a pulsed white beam. Among magnetic lenses (ii), (iii), and (iv), (ii) and (iv) modulate the field strength of a sextupole magnet continuously in time in order to tune the focusing force to the neutron wavelength, whereas lens (iii) switches the effective length of the sextupole magnet discretely by flipping the neutron spin state in time to tune the ratio of the converging and diverging lens lengths. The neutron lenses of (iii) have already been used in practice in the high-intensity and wide-range SANS instrument TAIKAN [24,25] at J-PARC. By increasing the numbers of sets of PM segments and spin flippers, such neutron lenses can handle a wider wavelength range. Moreover, the EM lens of (ii) requires a bulky power supply and a long magnet length because its field strength is lower than that of a superconducting magnet (SCM) or PM. However, a promising simulation result suggests that an additional static PM could shift the applicable wavelength range [26].

In addition to the advantages of the aforementioned magnetic refractive lens, a PM is lower in cost and more compact while still generating a sextupole field comparable to that of an SCM. On the other hand, a magnetic lens using an SCM is suitable for focusing a monochromatic beam [27–30], because the field strength modulation of a conventional SCM at the same frequency as the beam repetition rate is still impractical with current technology. While high-temperature-superconductor (HTS) magnets may overcome this problem, a pulsed HTS magnet would require considerable R&D on its fabrication with highly expensive HTS wires and on the handling of large amounts of stored energy and quench protection in addition to a high-power (MW-class) pulsed power supply. Suitable applications of the mod-PMSx (iv) may include TOF-type focusing SANS, scanning neutron-induced prompt gamma-ray analysis (PGA), neutron microscopy, and so forth, mainly using cold neutrons with a wide wavelength range. A prototype mod-PMSx lens has demonstrated satisfactory focusing performance for a pulsed beam over the wavelength range of 30–48 Å, with a distance of 4.8 m from the source point to the focus point [31]. Furthermore, the feasibility of its application to SANS experiments has been proven [32].

The main aim of this study is to determine the fine focusing capability over a wide wavelength range for a magnetic lens while suppressing the effect of chromatic aberration sufficiently for the spot size of the focused beam to remain equal to that of the source from the minimum wavelength $\lambda_{\min}$ up to the maximum wavelength $\lambda_{\max} = 2 \times \lambda_{\min}$. The value of $\lambda_{\max}/\lambda_{\min}$ for magnetic lenses has been about 1.5 [16]. Another aim is to establish a modular lens system consisting of a series of identical units for more practical applications to general neutron instruments. We have developed a second mod-PMSx lens that consists of three lens units, where each unit is nearly identical to the prototype. The focusing performance was evaluated and neutron image magnification was demonstrated using a pulsed beam with wavelengths of 27–55 Å [33,34]. The focusing principle and techniques used to realize the mod-PMSx are described in Sect. 2 and the results of focusing experiments are then reported in Sect. 3. We also report the results of neutron image magnification, which is one of the possible applications of the mod-PMSx, where we succeeded in magnifying an image by a factor of 4.

2.   Principle of mod-PMSx focusing of a pulsed beam

2.1.   Focusing principle

2.1.1.   Geometrical focus condition

Magnetic-lens focusing is based on the deflection force acting on a magnetic dipole moment μ of the neutron in a magnetic field gradient $\nabla|\mathbf{B}|$, which is known as the Stern–Gerlach effect:

$$M\frac{d^2\mathbf{r}}{dt^2} = \mp|\mu|\nabla|\mathbf{B}|, \tag{1}$$

where M and $\mathbf{r}$ are the mass and position vector of a neutron, respectively. In this paper, we assume that the local magnetic field is sufficiently strong to maintain the neutron spin parallel or antiparallel to the local magnetic field, which is known as the adiabatic spin transport condition [8]. The minus sign corresponds to the case in which the neutron spin is parallel to the magnetic field in each location, and vice versa. The sextupole field $\mathbf{B}_6$, which is perpendicular to the neutron-beam axis (z-axis) and given by Eq. (2), acts as a focusing lens for neutrons with parallel spin, where a positive constant value G_6 denotes the sextupole field strength:

$$|\mathbf{B}_6| = G_6/2\left(x^2 + y^2\right) \tag{2}$$

When $\mathbf{B} = \mathbf{B}_6$, the equations of motion of a neutron in the sextupole field for the cases of parallel and antiparallel spin are given by

$$\frac{d^2x}{dt^2} = \mp\omega^2 x, \quad \frac{d^2y}{dt^2} = \mp\omega^2 y, \quad \frac{d^2z}{dt^2} = 0. \tag{3}$$

where $\omega^2 = G_6|\mu M^{-1}|$. The neutrons with spin parallel to the local field oscillate around the beam axis and other neutrons diverge. Thus, the sextupole magnet works as a neutron lens based on this principle (Appendix A). In the following discussion, we assume that the beam is perfectly polarized in a direction parallel to the magnetic field.

We consider the case in which a neutron moves along the z-axis in drift space. The neutron is focused by a sextupole magnet with length L_m as it moves (Fig. 1). The beam forms an image on an image plane (P_3). Here, L_1 is the distance from the source point (P_0) to the lens entrance (P_1) and L_3 is the distance from the lens exit (P_2) to the image plane (P_3). The neutron velocity v can be approximated by the velocity along the z-axis, v_z, as follows: $v = \left(v_x^2 + v_y^2 + v_z^2\right)^{-1/2} \sim v_z$. The de Broglie wavelength λ of a neutron that moves a distance L in flight time t is given by

$$\lambda = \frac{h}{Mv_z} = \frac{h}{M}\frac{t}{L}, \tag{4}$$

where h is Planck's constant. The focusing condition is given by

$$\cot(\Omega \cdot L_\mathrm{m}) = \frac{\Omega\left(L_1 L_3 - 1/\Omega^2\right)}{L_1 + L_3} \quad (0 < \Omega \cdot L_\mathrm{m} < \pi), \tag{5}$$

where $\Omega \equiv \omega/v_z = \left(h^{-2}G_6 M|\mu|\lambda^2\right)^{-1/2}$. Its derivation is given in the Appendix. In the symmetric geometry with $L_1 = L_3 \equiv L^*$, the specific focus length L^* of the lens for an arbitrary λ in the case of sextupole field strength G_6 and magnet length L_m is given by

$$L^* = \frac{1}{\Omega}\cot\left(\frac{\Omega \cdot L_\mathrm{m}}{2}\right) \approx -\frac{L_\mathrm{m}}{6} + \frac{2}{\Omega^2 \cdot L_\mathrm{m}}, \tag{6}$$

The approximation has an error of less than 1% when L_m is up to around 30% of the total focusing distance $L_\mathrm{tot} = L_\mathrm{m} + 2L^*$ (thin-lens approximation). When the source diameter d_0, G_6, L_m, and λ
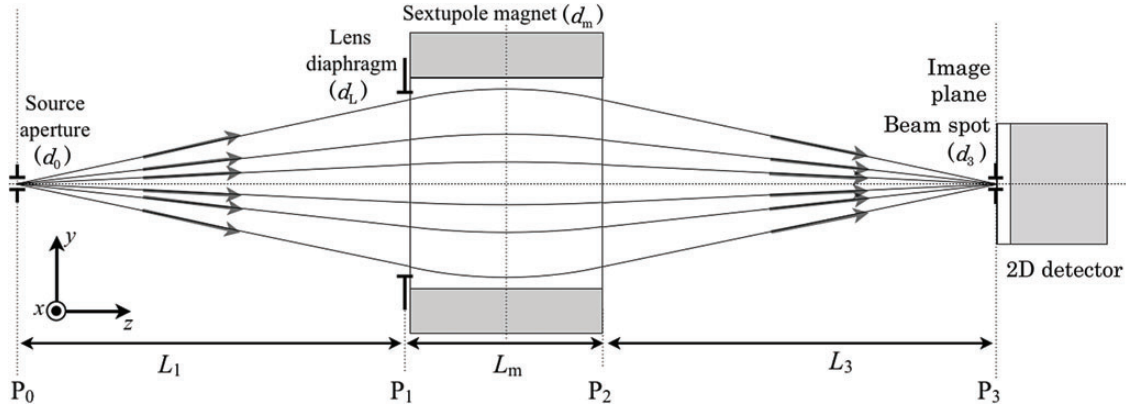
Fig. 1. Schematic side view of a neutron trajectory.

are given, the beam spot diameter d_3 of the focused beam on the image plane (P_3) can be obtained as

$$d_3 = \frac{d_0}{\Omega \cdot L_1 \sin(\Omega \cdot L_m) - \cos(\Omega \cdot L_m)}. \tag{7}$$

The magnification α is defined as the ratio of d_3 to d_0; $\alpha \equiv d_3/d_0 \sim L_3/L_1$. This approximation also corresponds to the thin-lens approximation.

2.1.2.   TOF instrumentation

L^* depends on λ, which is known as the chromatic aberration effect. L^* can be made constant over the wide wavelength range of the pulsed beam by changing G_6 as follows:

$$G_6 \propto \lambda^{-2} \propto t^{-2}. \tag{8}$$

We write G_{6_high} and G_{6_low} for G_6 when neutrons with the minimum wavelength λ_{min} and maximum wavelength λ_{max} are focused in a distance of L^*, respectively. By introducing a new parameter, $\kappa_\lambda \equiv \lambda_{max}/\lambda_{min}$, to indicate the width of the wavelength range, the minimal G_6 modulation range κ_{G_6}, which is defined as the ratio of G_{6_high} to G_{6_low}, is given by

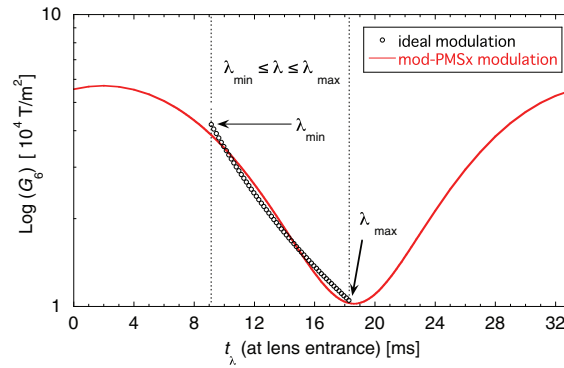$$\kappa_{G_6} = G_{6\_high}/G_{6\_low} = (\lambda_{max}/\lambda_{min})^2 = \kappa_\lambda^2. \tag{9}$$

The dynamic modulation range should be considerably wider than the minimal modulation range. While G_6 of a sextupole EM can be easily tuned, that of a PM can also be modulated as follows. The sextupole magnet configuration of the mod-PMSx is the extended-Halbach-type [35,36] (Fig. 2(b)). The sextupole ring is divided into two nested coaxial rings, where the inner ring is fixed and the outer ring can be rotated continuously, which we call a rotating double-ring structure (Fig. 2(c)). The sextupole field strength G_6 is modulated as a cosine function of the rotation angle:

$$G_6(t) = G_6^{cnt} + G_6^{amp} \cos(2\pi f_b t - \delta), \tag{10}$$

where G_6^{cnt} and G_6^{amp} are positive constant values and f_b is a beam repetition rate. By synchronizing the modulation of G_6 with the beam pulse repetition, part of the descending region of the cosine modulation function can approximate the ideal modulation given by Eq. (8). Figure 3 shows the field strengths as a function of time of flight t_λ at the lens position where the ordinate is on a log scale. The dots show the required (ideal) field strengths to keep the focus lengths constant at each wavelength. The sinusoidal curve shows the modulation of the mod-PMSx whose phase is adjusted to match the required strength. The applicable time range for a single beam pulse at the lens position is
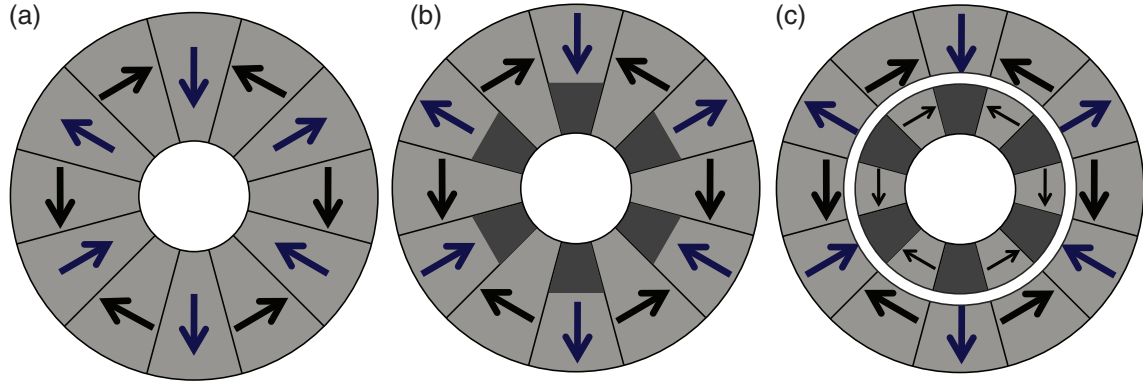
Fig. 2. Sextupole magnetic configurations: (a) normal Halbach-type, (b) extended-Halbach-type, and (c) rotating double-ring structure. The arrows show the easy axis of each magnet segment. The light/dark gray areas represent the permanent magnet and soft iron material, respectively. A neutron beam passes through the inner bore where the sextupole field is generated.

Fig. 3. Schematic diagram of synchronized modulation of sextupole field strength with a beam pulse.

around $T_b/8 < t < T_b/2$, where $T_b = f_b^{-1}$. Therefore, the dynamic modulation range of G_6 should be considerably wider than the minimal G_6 range from G_{6_high} to G_{6_low}. Note that the frequency of the outer-ring rotation f_{rot} is one-third of the beam repetition rate because of the threefold symmetry of a sextupole field: $f_{\mathrm{rot}} = f_b/3$.

2.1.3. *Gain in beam flux*

A mod-PMSx lens increases the neutron-beam flux on the transverse plane, $\phi_b\ \mathrm{s}^{-1}\,\mathrm{cm}^{-1}\,\text{Å}^{-1}$, while the injected beam current $I_b\ \mathrm{s}^{-1}\,\text{Å}^{-1}$ is conserved. The beam current I_b is proportional to the solid angle defined by the source aperture and the lens diaphragm, and depends on L_1 and the lens diaphragm diameter d_L:

$$I_b \propto I_0\,(d_L/L_1)^2\,, \tag{11}$$

where I_0 is the beam current passing through the source aperture, taking the duty cycle into account. The lens diaphragm diameter should satisfy

$$d_L^2 + ((d_L + d_0)\,/\,(\Omega \cdot L_1))^2 < d_m^2, \tag{12}$$
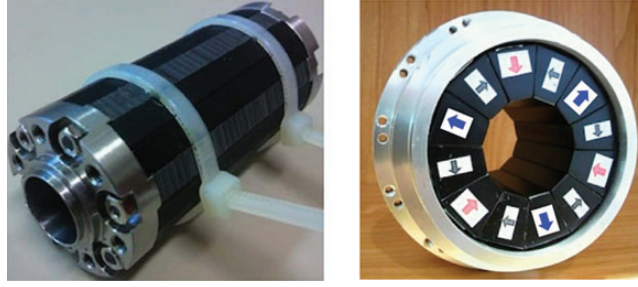
Fig. 4. Inner (left) and outer (right) rings of the unit of the mod-PMSx. The short light gray parts in the inner ring are laminated Permendur poles. The cable ties were used to maintain the shape of the inner ring until the adhesive solidified.

where d_0 and d_m are the diameters of the source aperture and sextupole magnet bore, respectively. A shorter focus length results in a higher beam current. A magnifying optical geometry ($L_1 < L_3$) also provides a higher beam current.

We write $\phi_{\text{focus}}(\lambda)$ for the flux of the focused beam at the image plane and $\phi_{\text{no-focus}}(\lambda)$ for the beam flux at the image plane without the lens but with the lens diaphragm. We define the gain in beam flux per unit wavelength $\zeta_{\text{f}}(\lambda)$ as the ratio of the beam flux $\phi_{\text{focus}}(\lambda)/\phi_{\text{no-focus}}(\lambda)$. Since the injected beam current is common to both setups, $\zeta_{\text{f}}(\lambda)$ is the ratio of the beam spot size at the image plane:

$$\zeta_{\text{f}}(\lambda) = \left(\frac{d_{\text{L}}}{d_3}\right)^2 \left(\frac{L_{\text{tot}}}{L_1}\right)^2, \tag{13}$$

where $L_{\text{tot}} = L_1 + L_m + L_3$.

2.2.   Development of mod-PMSx

We developed the mod-PMSx on the basis of the foregoing focusing principle so that a very cold neutron (VCN) pulsed beam of 30 Hz with a wavelength range from 27 to 55 Å ($\kappa_\lambda \sim 2$) can be focused in a total focusing distance of 2 m. (i) The sextupole magnet configuration was designed to have a strong sextupole field and a wide dynamic modulation range. (ii) To ensure sufficient magnetic strength to achieve a total focusing distance of $\sim$2 m, the mod-PMSx lens consists of three identical and serially connected mod-PMSx units. (iii) A small torque for rotation was achieved by developing a novel magnetic torque canceler, resulting in a compact device. These three points are described below.

2.2.1.   Sextupole magnet design

The extended-Halbach-type configuration (Fig. 2(b)) is a modified Halbach-type configuration (Fig. 2(a)) [37] produced by replacing the PM segments at the pole positions close to the beam bore with soft-magnetic-material segments [31,38,39]. The magnetically saturated poles significantly enhance the maximum field strength $G_{6\text{max}} = G_6^{\text{cnt}} + G_6^{\text{amp}}$ (Eq. (10)) and expand the dynamic modulation range of G_6. The inner ring of the mod-PMSx consists of 18 segments; every third segment at the six pole positions consists of the high-saturation-magnetization material Vanadium Permendur (Fe–Co–V; 49%:49%:2%) and the other segments are strong permanent NdFeB magnets (Figs. 2(b) and 4 (left)). The outer ring consists of 12 NdFeB magnet segments (Fig. 4 (right)). The bore diameter d_m and the outer diameter of the inner ring are 15 mm and 35 mm, respectively. The inner and outer diameters of the outer ring are 37 mm and 76 mm, respectively. The thickness ratio of the

inner ring to the outer ring significantly affects the dynamic modulation range of G_6. The ratio was designed for a beam of $\kappa_{G_6} = G_{6\_high}/G_{6\_low} = \kappa_\lambda^2 = (\lambda_{max}/\lambda_{min})^2 = 4$. The dynamic modulation ranges of G_6 of the three fabricated units were measured as $G_6 = 0.99 \times 10^4$–$5.51 \times 10^4\,\mathrm{Tm}^{-2}$, $G_6 = 0.80 \times 10^4$–$5.46 \times 10^4\,\mathrm{Tm}^{-2}$, and 1.06×10^4–$5.86 \times 10^4\,\mathrm{Tm}^{-2}$, which are wider than the value of $\kappa_{G_6} = 4$ by a considerable margin. To avoid thermal demagnetization of the magnets, their temperatures have to be kept low. Since the Permendur alloy is immersed in the modulated magnetic field, it generates heat from eddy current loss and hysteresis loss. Thus, the Permendur segments were laminated with 2 mm-thick slices to decrease eddy current loss, and they were annealed after all the mechanical processes to minimize hysteresis loss. Stacked Permendur slices with a hole diameter of 3 mm were glued together with a strong two-component acrylic adhesive and then pierced and tied together with iron rods with a diameter of 3 mm. In spite of there being no insulator between the slices other than the adhesive, the resistance of the laminated segments was increased to more than 10^4 times that of the bulk segments. The magnet and the laminated Permendur segments were glued together with the same adhesive and tightly wound with Kevlar$^{\textregistered}$ poly-paraphenylene terephthalamide string [40] to increase the mechanical strength of the inner ring. The magnets of the outer ring are held in a cylindrical case and fixed with set screws. The increase in temperature due to heating from the environment during continuous operation was suppressed to $25\,^{\circ}\mathrm{C}$.

Among the fabricated magnetic lenses developed so far, this mod-PMSx has the highest G_{6max} (Table 1 and Fig. 5). The maximum field strength G_{6max} of the mod-PMSx is almost half that of an SCM for the same d_m, although it would be difficult to fabricate an SCM with such a small bore diameter. The relatively small d_m of 15 mm was chosen for the mod-PMSx lens because of the need to focus the neutrons of the VCN beam in a distance of $\sim$2 m using magnets with a small volume. Since the field gradient of a Halbach-type permanent sextupole magnet is inversely proportional to d_m^2, the magnet length L_m increases in proportion to d_m^2 for a given focusing strength. The bore diameter should be designed to achieve the target focus length (Eq. (6)) and to maximize the beam current (Eq. (11)) under the constraints of the mod-PMSx device size in the neutron instrument and the size of the available rare-earth magnets.

Next, let us consider the performance of the magnetic lenses. The specific focus length L^* is dominated by the right-hand term in Eq. (6) and is nearly inversely proportional to $G_{6max}L_m$. Because the focused beam flux is proportional to a solid angle of the lens aperture from the focal point, approximately $(d_m/L^*)^2$, the figure of merit of a magnetic lens, F, can be evaluated with $(G_{6max}d_m L_m)^2$ (Table 1). According to this index, the mod-PMSx is not superior among these fabricated magnetic lenses due to its compactness, which means small L_m. The L_m of magnetic lenses, however, can be extended easily, thus it is fair to compare the intrinsic focusing performances with the same L_m. Therefore, we define it as $F^\dagger = (G_{6max}d_m)^2$ for this purpose and the mod-PMSx has the highest $F^\dagger$. This means that the available beam flux with the mod-PMSx can be effectively increased by adding more lens units along the beam axis.

2.2.2.   Modular lens system

Once a sextupole magnet design including the field strength G_6 is fixed, the magnet length L_m is obtained by solving Eq. (5) to satisfy the required instrument size L_{tot}. A modular structure with identical small units stacked in series can realize almost any value of L_m, which makes the mod-PMSx lens system easily adaptable to various requirements [33,34]. A total focusing length of less than 2 m was achieved for neutrons of wavelengths from 27 to 55 Å by stacking three identical units in series along the beam line, where the single-unit inner and outer ring lengths are 66 mm. The size

Table 1. List of fabricated sextupole magnet lenses. PM, SCM, EM, and SF stand for permanent magnet, superconducting magnet, electromagnet, and spin flipper, respectively.

No.	Magnet type	Year	Bore diameter d_m [mm]	Field strength G_{6max} [Tm^{-2}]	Effective magnet length L_m [m]	F ($G_{6max}{}^2 d_m{}^2 L_m{}^2$) [$10^4$ T^2]	$F^\dagger$ ($G_{6max}{}^2 d_m{}^2$) [10^4 T^{2}m^2]	Applicable beam type
1	PM [8]	1998	9	32 000	2	8.3	2.1	Monochro-matic
2	PM [9]	2006	30	10 660	2.4	15	2.6	Monochro-matic
3	PM [41]	2007	30	11 480	1.2	4.3	3.0	Monochro-matic
4	SCM [27,28]	2003	46.8	12 800	2	36	9.0	Monochro-matic
5	EM [13]	2004	26	7500	2	3.8	1.0	Pulsed
6	PM+SF [14]	2002	9	35 000	2+1	22	2.5	Pulsed
7	PM+SF [25]	2009	20	36 000	0.26	0.88	13.0	Pulsed
			25	23 200	0.8	5.4	8.4	
8	PM+SF [9,16]	2010	35	10 660	1.5 + 0.4 + 0.5	20	3.5	Pulsed
9	Mod-PMSx [33,34]	2011	15	56 100 (average)	0.198 (0.066 × 3)	0.69	17.7	Pulsed
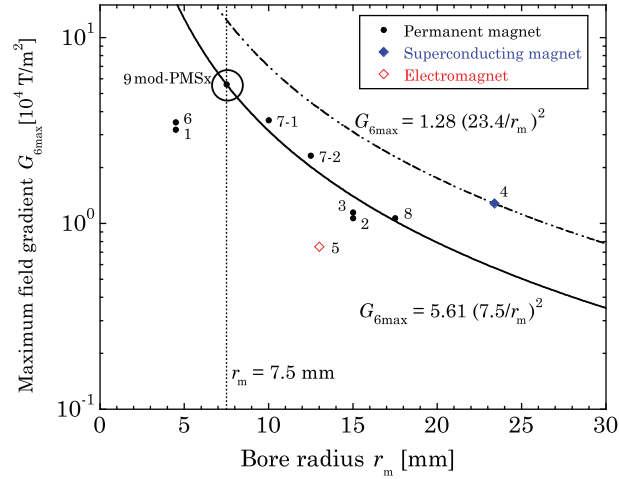
Fig. 5. Sextupole field strength plotted against bore radius of the mod-PMSx compared with plots for other fabricated magnetic lenses. Closed circles represent sextupoles made of a permanent magnet. Closed and open rhombuses represent sextupoles made of a superconducting magnet and an electromagnet, respectively. Numbers in the plot correspond to those in Table 1.
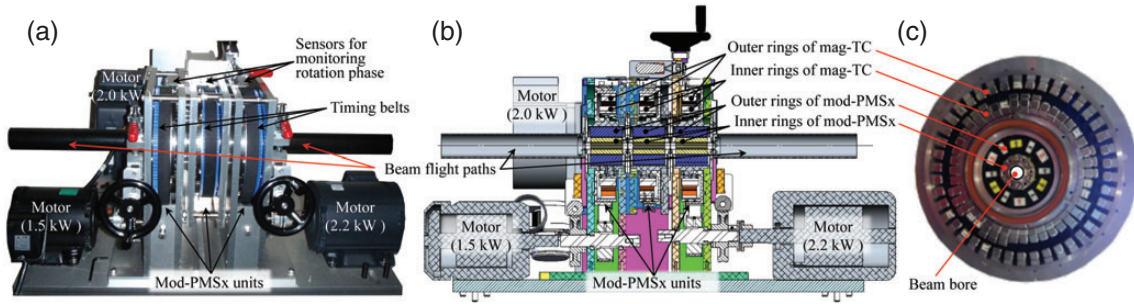
Fig. 6. Mod-PMSx: (a) external view, (b) sectional view taken along the beam line, and (c) sectional view taken perpendicular to the beam line.

of the single unit was the size of the available rare-earth magnets, which was limited by their ingot size. The spacing between two units is 22 mm. O-rings are used between units to maintain the He gas environment in the bore, which is part of the flight path of the beam. Each unit is driven by a different motor and its rotation phase is controlled independently of the other units. When each mod-PMSx unit is sufficiently thin to satisfy the thin-lens approximation, the effective focus length L_{eff}^{*} of the assembled mod-PMSx with n lens units is given by

$$L_{\text{eff}}^{*} = \left(\sum_{i=1}^{n} \frac{1}{L_i^{*}} \right)^{-1}, \tag{14}$$

where L_i^{*} is the focus length of the ith unit given by Eq. (6). The effective focus length can be shortened to a practical distance for neutrons with the same or a shorter wavelength range, such as cold neutrons, by cascading single units. External and sectional views of the realized triplet mod-PMSx lens are shown in Figs. 6(a) and (b), respectively.

2.2.3. Magnetic torque canceler

Figure 7 shows the measured torques for the outer-ring rotation of the mod-PMSx. Although the magnitude is large due to the high magnetic field, the torque integrated over one revolution is basically
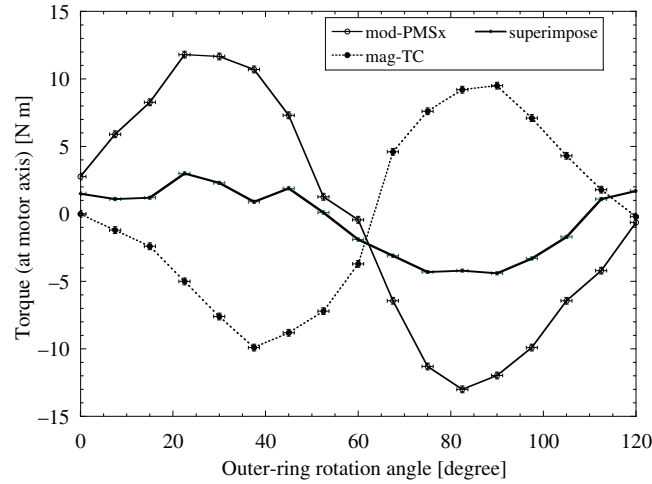
Fig. 7. Torque for the mod-PMSx modulation per unit. The installed mag-TC, which generated torque nearly identical in magnitude but of opposite polarity, canceled the mod-PMSx torque, resulting in suppressed net torque during operation.

zero, which is analogous to cogging torque. Therefore, smoothing the torque reduces the peak power required for the operation. Thus, we installed a novel magnetic torque canceler (mag-TC) around the mod-PMSx double rings (Fig. 6(c)). It consists of a rotating double-ring structure similar to the mod-PMSx and generates torque of almost the same magnitude as the mod-PMSx but with the opposite polarity (the broken line in Fig. 7). The outer rings of the mod-PMSx and mag-TC are fixed together and linked to the motor axis with a timing belt with a 1/3 reduction ratio. Owing to the threefold symmetry of a sextupole field, the motor axis rotates at the same frequency as the beam repetition rate. However, the inner rings of the mod-PMSx and mag-TC are fixed to the unit frame. The magnet configuration of the mag-TC was designed to cancel the measured mod-PMSx torque, whose second harmonic component was about 30% of that of the fundamental component. Because of the large diameter of the TC, cheap off-the-shelf magnet bricks can generate sufficient anti-torque. Both the inner and outer rings consist of 42 NbFeB magnet bricks (10 mm × 10 mm × 40 mm) with three periods of the following easy axis orientations along the angular axis: →→→→→→↑↑↑←←↓↓↓ (→:↑:←:↓= 6 : 3 : 2 : 3). This sequence generates the second harmonic component. The bricks with an easy axis parallel to the radial direction in the inner ring were extended to a height of 15 mm [34]. Because of cancelation by the mag-TC torque, the required torque for the operation became a quarter of that for the original set of mod-PMSx rings. Since the reduction ratio was 1/3, the maximum torque at the motor axis became 3.0 Nm. The original torques of mod-PMSx and mag-TC, and the canceled torque are shown in Fig. 7. The three mod-PMSx units are driven by 1.5 kW, 2.0 kW, and 2.2 kW controllable interior permanent-magnet (IPM) motors. The fabricated triplet mod-PMSx lens system including the motors is 150 kg in weight and 976 mm × 560 mm × 520 mm in size. Each lens unit is only 25 kg.

3. Experiment

We performed a focusing test on the fabricated triplet mod-PMSx and a demonstration of neutron image magnification at the PF2-VCN beam line at Institut Laue-Langevin (ILL) in Grenoble, France [42]. The bore diameter d_m for the mod-PMSx is 15 mm, the effective magnet length L_m is 198 mm, the three-unit sextupole field strengths are in the ranges of $G_6 = 0.99 \times 10^4 -$
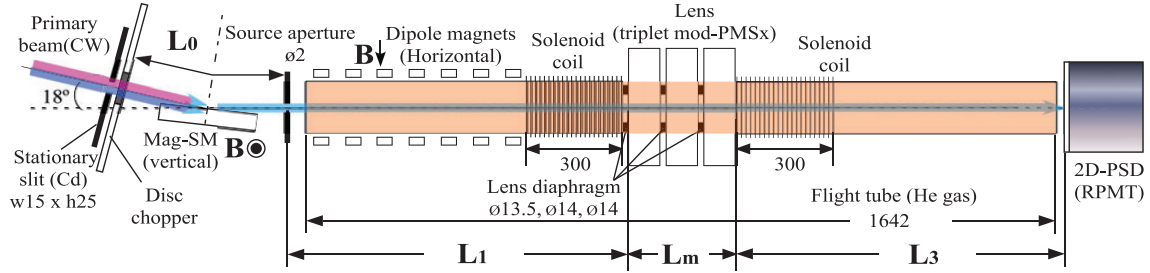
Fig. 8. Schematic top view of the setup for the focusing test in units of mm.

Table 2. Optical geometries used (in units of mm).

Geometry	L_0	L_1	L'_m	L_3	L_{tot}	L_{full}
Focusing	394 ± 2	788 ± 2	264 ± 0.5	788 ± 2	1840 ± 2	2234 ± 2
No focusing	349 ± 2	818 ± 2				1167 ± 2

$5.51 \times 10^4 \, \mathrm{Tm}^{-2}$, $G_6 = 0.80 \times 10^4 - 5.46 \times 10^4 \, \mathrm{Tm}^{-2}$, and $1.06 \times 10^4 - 5.86 \times 10^4 \, \mathrm{Tm}^{-2}$, and the maximum beam repetition rate f_b is 30 Hz. We measured beam profiles with and without focusing by using the mod-PMSx to evaluate the gain in beam flux.

3.1.   Pulsed beam focusing test

3.1.1.   Experimental setup

The primary beam provided at the VCN beam line is a continuous beam of unpolarized VCNs over the wavelength range of 20–400 Å. The incident angle is 18° to the VCN cabin. The wavelength range of 27–55 Å was selected by considering the intensity distribution. Although a VCN beam is less typical than a cold or thermal neutron beam in the present-day major field of neutron science, the VCN beam made this focusing test easy because of the shorter focus length given by Eq. (6). The schematic setup and the significant lengths in the focusing geometry are shown in Fig. 8 and Table 2, respectively.

At the uppermost stream, the continuous beam was pulsed at 30 Hz using a disc chopper coated with paint comprising 60 wt% Gd_2O_3. The pulsing duty cycle was 2.3% for the wavelength resolution $d\lambda/\lambda \leq 5\%$ with the focusing geometry. A reflective photosensor fixed to the chopper base and a marker on the rotating disc generated a start signal for every beam pulse for TOF measurement. A magnetic supermirror of $Fe/SiGe_3$ multilayers with $m = 3.5$ Qc [43] only reflects neutrons with wavelengths of above 27 Å with an incident angle of 9°. Fully magnetized by a 300 G vertical dipole field, the supermirror also acted as a spin polarizer. Because only neutrons in the parallel-spin state are focused by the magnetic lens, the other neutrons need to be excluded in advance. The polarization has a linear dependence on the neutron wavelength and ranged from 80 to 90% over the selected wavelength range with an incident angle of 9° (Fig. 9), which was measured using the Platypus [44] TOF neutron reflectometer at the OPAL reactor. The pulsed, polarized, and wavelength-selected neutron beam was collimated by a Cd source aperture of 2 mm diameter and propagated to the mod-PMSx lens. The polarization was maintained up to the mod-PMSx entrance by a seamless magnetic field of at least 15 G, maintaining the adiabatic conditions. The second solenoid coil maintained the polarization at the exit of the mod-PMSx. In the focusing experiment we did not require a polarized beam at the detector and thus no magnetic field was provided between the second solenoid coil and the
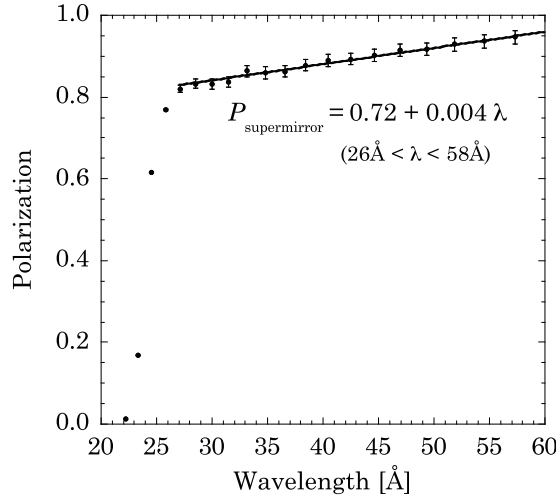
Fig. 9. Polarization of the supermirror $P_{\text{supermirror}}$ against wavelength λ.

detector. The mod-PMSx and detector were installed to satisfy the optical arrangement required for a magnification of $\alpha = 1$, defined in Sect. 2.1.1. We used an RPMT detector [45], which is a 2D position-sensitive detector composed of a ^{6}LiF/ZnS scintillation screen and a photomultiplier tube (PMT). The RPMT has the ability of TOF measurement by using the start signal from the chopper. The spatial resolution is around 1.0 mm in the x- and y-directions and the diameter of the detection area is more than 100 mm. The wavelength dependence of the detection efficiency was not taken into account in the measured neutron currents because the beam flux was compared at the same wavelengths.

The synchronization among the rotations of the three lens units and the chopper signal was controlled by a phase-locked loop (PLL) circuit. The rotation phases of the three lens units were separately monitored by photosensors. The three signals and the chopper signal were synchronized with the master clock (CLK) in the PLL circuit. The measured timing jitters of the three lens units and the chopper rotation at 30 Hz, referring to the CLK, were sufficiently small. The lens jitters were less than 0.2 ms, while the chopper jitter was 0.1 ms. Since absolute phase measurements were difficult, the optimum synchronizing delays that provide the focused beam with the smallest blur were obtained by a scanning method.

The wavelength was obtained from the modified TOF method using the following formula:

$$\lambda = \frac{h}{M} \frac{(t - t_0)}{L_{\text{full}}},$$

$$L_{\text{full}} = L_0 + L_{\text{tot}} = L_0 + L_1 + L_{\text{m}} + L_3, \tag{15}$$

where t_0 is the offset and L_0 is the distance from the chopper disc to the source aperture. The measured value of t_0 in this experiment was $+0.5 \pm 0.3$ ms. While the error of t_0 increased $d\lambda/\lambda$ by at most 0.4%, the maximum $d\lambda/\lambda$ is 5.4% with the focusing geometry.

The optimum phase delays of the three lens units from upstream, δ_1, δ_2, and δ_3, and the effective focus length L_{eff}^* were estimated by the least-squares method using Eqs. (6), (10), and (14) with the measured G_6 of the three units: $L_{\text{eff}}^* = 798$ mm; $\delta_1 \equiv t_{\text{s}}$ ms, $\delta_2 = t_{\text{s}} - 0.63$ ms, and $\delta_3 = t_{\text{s}} - 2.19$ ms.

We measured the beam profile, i.e., the beam flux distribution on the transverse plane, with $L_{\text{eff}}^* = 798$ mm and the relative phases fixed while changing t_{s}. The observed beam profiles were

projected to the x- and y-axes and fitted by a 1D single Gaussian distribution function. We evaluated the ellipsoidal beam spot diameter along each axis d_{3i} ($i = x$ and y) as follows:

$$d_{3i} = \mathrm{FWHM}_i = \sqrt{8\ln(2)} \times \sigma_i, \tag{16}$$

where σ_i^2 ($i = x$ and y) are the variances of the 1D single Gaussian along the x- and y-axes, respectively. The beam spot size was determined from the ellipsoidal area using d_{3x} and d_{3y}. The beam current was obtained by integrating the measured neutron current over the detection area. The beam flux on the transverse plane was calculated by dividing the beam current by the measured ellipsoidal beam spot area. After t_s was determined by the phase scan, L_{eff}^* was determined to be 788 mm in the same way by changing L_3 by moving the detector with t_s fixed. Note that the magnet distance L_m' here included not only the effective magnet length L_m but also the gap distance, namely, $L_m' = (66 + 22) \times 3 = 264$ mm. Finally, the optical geometry for $\alpha = 1$ was determined, as shown in Table 2. The neutron flight path from the source aperture to the detector surface was windowless and filled with He gas to avoid attenuation of the VCN beam flux in air. In accordance with Eq. (12), Cd lens diaphragms of diameter 13.5 mm, 14.0 mm, and 14.0 mm were installed at each lens entrance to prevent neutrons from hitting magnets.

Because of the geometrical constraint, the focused beam profiles were compared with the beam profiles measured at the lens entrance with the detector installed instead of the mod-PMSx: $L_{\mathrm{full}} = L_0 + L_1 = 1167$ mm (Table 2). The no-focusing geometry resulted in the wavelength resolution $d\lambda/\lambda \leq 10.3\%$, where the error of t_0 was included. A lens diaphragm of diameter 13.5 mm was installed on the detector surface at almost the same position as the entrance of the first mod-PMSx unit. Because the primary VCN beam is composed of two peaks, the projections to the x- and y-axes were each fitted by a 1D double Gaussian distribution function. We evaluated the ellipsoidal beam spot diameter along the x-axis d_{3x} as follows:

$$\begin{aligned} d_{3x} &= (\mathrm{FWHM}_{x1} + \mathrm{FWHM}_{x2})/2 + |x_{02} - x_{01}|, \\ &= \sqrt{2\ln(2)}(\sigma_{x1} + \sigma_{x2}) + |x_{02} - x_{01}| \end{aligned} \tag{17}$$

where σ_{x1} and σ_{x2} are the variances and x_{01} and x_{02} are the centroids of the two peaks of the 1D double Gaussians. The calculation along the y-axis follows the same procedure. The beam spot size was determined from the ellipsoidal area using d_{3x} and d_{3y} [33].

Note that the flight path was in air in the measurement with the no-focusing geometry. Therefore, the difference between these flight paths was considered. The transmission of the VCN in air T as a function of the flight path length L m and wavelength λ Å was determined by measurement as

$$T(L, \lambda) = \exp(-a\lambda L), \tag{18}$$

where a was measured to be $0.0129 \pm 0.0001\,\mathrm{m^{-1}\mathring{A}^{-1}}$. On the other hand, the measured attenuation of the VCN beam flux in He gas was negligible. Finally, only the correction of the attenuation in air in the measurement with the no-focusing geometry was made and added to the results reported previously [33]. The beam current and flux were obtained in the same way as in the measurement with the focusing geometry. Furthermore, the gain in beam flux of the mod-PMSx at each wavelength ζ followed Eq. (13), namely,

$$\zeta = \frac{\phi_{\mathrm{focus}}}{\phi_{\mathrm{no\text{-}focus}}} = \frac{d_{3x}d_{3y}}{d_{L_1}^2}\frac{\phi_{\mathrm{focus}}}{\phi_{\mathrm{diaphragm}}}, \tag{19}$$

where ϕ_{focus} is the beam flux calculated using the measured beam current and beam spot size at the focus point with the focusing geometry, and $\phi_{\mathrm{diaphragm}}$ is the beam flux calculated using the measured
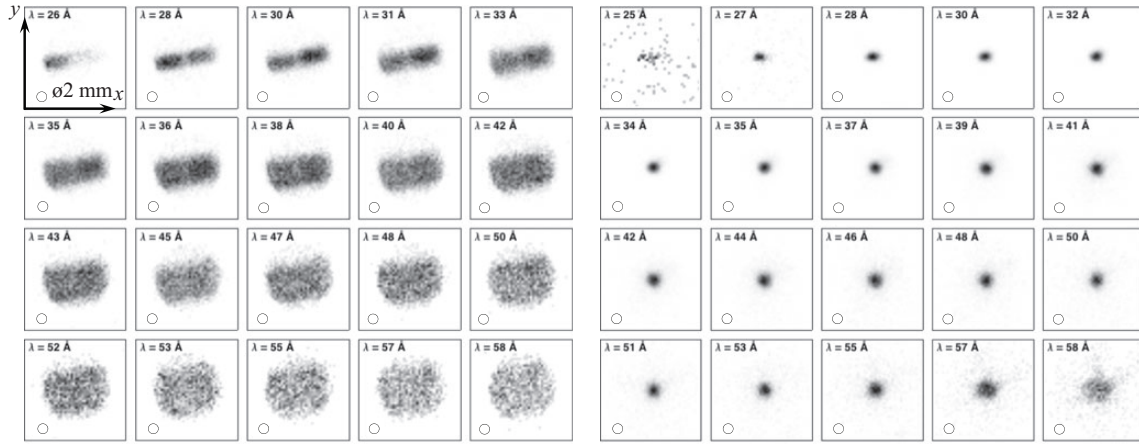
Fig. 10. Comparison of the beam spot size and flux between (left) unfocused and (right) focused beams measured at the lens entrance and on the image plane, respectively. Every frame indicates 20 mm × 20 mm in real space. The open circle placed in each box indicates the source aperture of 2 mm diameter. The beam entering the mod-PMSx had a structure because of the neutron-beam guide from the moderator of the high-flux reactor to the VCN cabin. The beam was effectively focused by the mod-PMSx lens within the target wavelength range of 27–55 Å.

beam current and beam spot size at the first lens diaphragm position with the no-focusing geometry. $\phi_{\text{no-focus}}$ is the beam flux calculated using the propagation of $\phi_{\text{diaphragm}}$ to the detection point of the focusing geometry.

3.1.2. Results

The beam fluxes focused and intensified by the mod-PMSx were measured at the image plane. They were compared with those measured at the lens entrance position, as shown in Fig. 10. Within the target wavelength range of 27–55 Å, the beam spot size at each wavelength remained much smaller (Fig. 10 (right)) than the beam spot size at the entrance (Fig. 10 (left)). On the other hand, the spot sizes of beams with a wavelength outside the range exhibited an aberration effect, and the beam spot gradually became larger than the size of the focused beam. The beam guide from the cold moderator to the VCN cabin caused a structure to appear in the beam profiles, which was observed in the measurement of the unfocused beam at shorter wavelengths (Fig. 10 (left)). The vertical beam guide was gradually bent by 90° from the vertical exit of the moderator to the horizontal beam line [46]. Therefore, the beam divergence along the y-axis was smaller than that of the beam collimated by the source aperture and the first lens diaphragm at shorter wavelengths. Meanwhile, the beam divergence along the x-axis was larger than that of the collimated beam. Thus, the diaphragm was fully illuminated only along the x-axis.

The diameters of the measured beam spots with the focusing and no-focusing geometries were evaluated using Eqs. (16) and (17), respectively. The unfocused beam diameter along the y-axis showed clear wavelength dependence, which originated from the linear dependence of the critical angle of the Ni coating on the wavelength and the complex shape of the guide. However, the beam diameter along the x-axis was determined by the diameter of the first lens diaphragm and was independent of the wavelength (Fig. 11 (left)). Although the diameter of the focused beam showed slight wavelength dependence along both axes even within the target wavelength range, the standard deviations along the x- and y-axes within the target wavelength range were both as small as 10% (Fig. 11 (right)). The linear dependence of the beam spot diameter along the y-axis up to a wavelength of 45 Å, however,
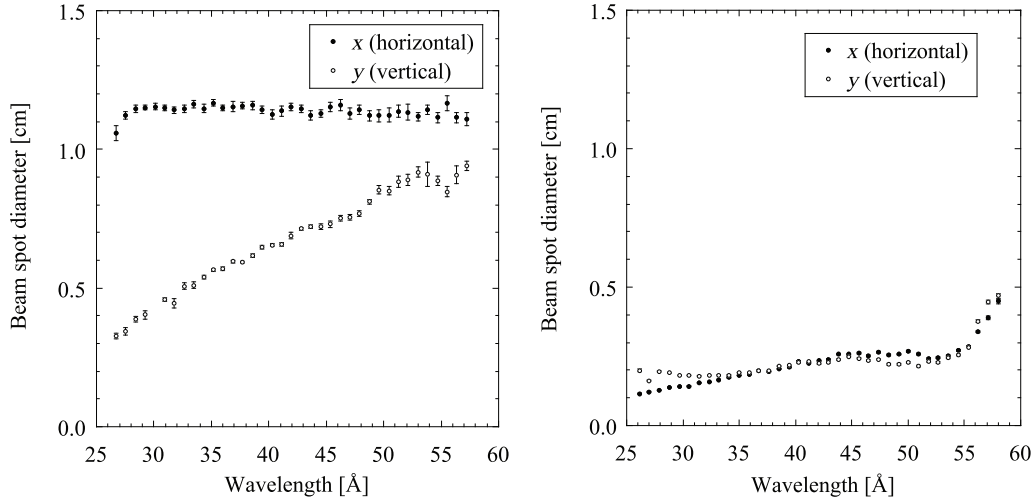
Fig. 11. Diameters of ellipsoidal beam spots along x- and y-axes in the cases of (left) unfocused beam and (right) beam focused by the mod-PMSx lens.
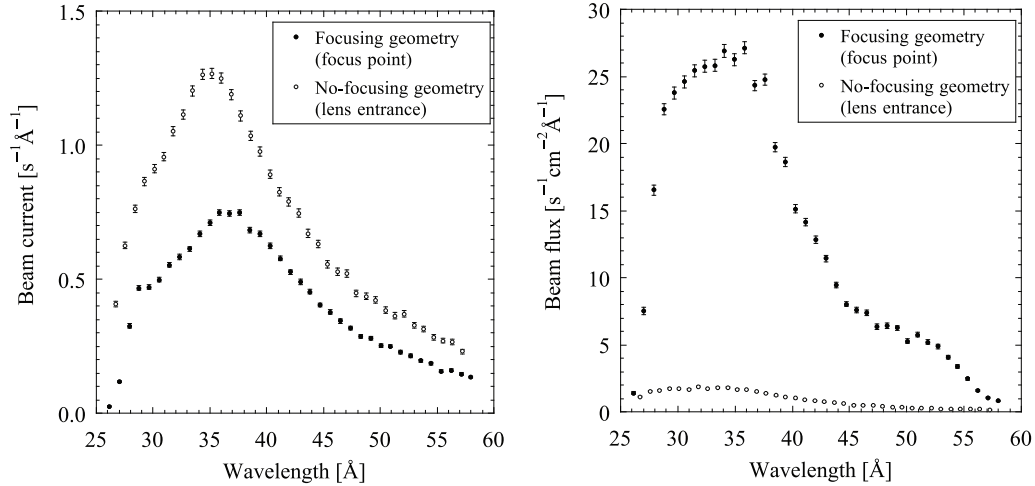

Fig. 12. Beam current (left) and beam flux (right) on the transverse plane measured in the no-focusing and focusing geometries.

indicated the effect of the beam guide on the beam structure, similarly to in the case of an unfocused beam. Overfocusing at wavelengths of above 55 Å caused abrupt increases in the diameter along both axes.

The peak beam current of the focused beam was observed at 36 Å (Fig. 12 (left)). The intensity of the beam flux at each wavelength increased significantly in the target wavelength range (Fig. 12 (right)). The integrated beam flux was intensified by a factor of 43 according to Eq. (19). Note that the attenuation in air was taken into account in the estimation, while the wavelength-dependent detection efficiency was not taken into account.

3.2. *Demonstration of neutron microscopy*

A demonstration of neutron image magnification was performed using the focusing test setup. We observed two neutron images of the same mask using different optical arrangements having magnifications of $\alpha = 1$ and $\alpha = 5$. The definition of the magnification α is given in Sect. 2.1.1.
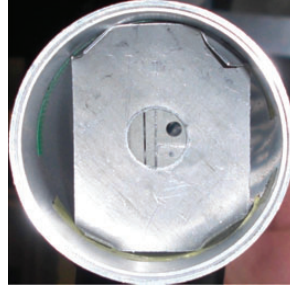
Fig. 13. Sample mask fixed inside the 55 mm-diameter flight tube with holes of 1 mm and 3.5 mm diameter and a 0.5 mm-wide slit.
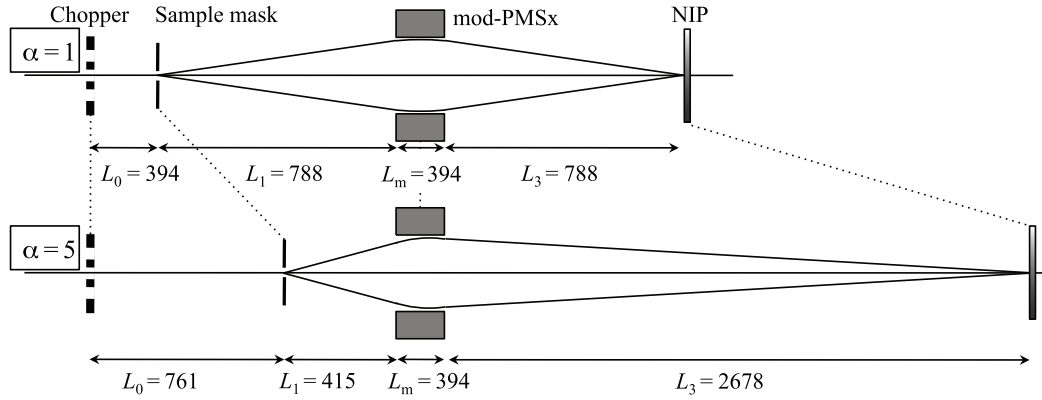
Fig. 14. Optical arrangements for the magnifications of $\alpha = 1$ and $\alpha = 5$. The optical arrangement was varied by moving the positions of the sample mask and NIP while the position of the mod-PMSx was fixed.

3.2.1. Experimental setup

The measurement with the optical arrangement for $\alpha = 1$ was performed with a setup similar to that in the focusing test (Fig. 8, Table 2), except for the source aperture and detector. The source aperture was replaced with a sample mask having holes of 1 mm and 3.5 mm diameter and a 0.5 mm-wide slit (Fig. 13). The RPMT detector was replaced with a neutron imaging plate (NIP) that has no time resolution but a high spatial resolution of $\sim 50\,\mu$m. Additionally, the locations of the sample mask and NIP were adjusted to obtain a magnification of unity ($\alpha = 1$).

Furthermore, the locations of the sample mask and NIP were moved in accordance with Eq. (7) in the measurement for $\alpha = 5.0 \pm 0.6$ using the effective value of G_6 evaluated by the focusing test (Fig. 14, Table 3). In this case, the sample mask was installed inside the flight tube. In both measurements, a flight tube filled with He gas was installed from the source point to each detection surface. The attenuation of the VCN beam flux in He gas was ignored.

In the same way as for the focusing geometry in the focusing test, the images of two holes observed in both measurements were projected along the x- and y-axes and were fitted by a 1D single Gaussian function (Eq. (16)). Because the magnified images were affected by the primary beam structure, the beam spot sizes could not be directly compared. Therefore, the distances between the centers of the two circles were compared.

3.2.2. Results

The magnified image obtained with the optical arrangement for $\alpha = 5$ was compared with that observed for $\alpha = 1$ (Fig. 15). The distance between the two circles for $\alpha = 5$ was 4.1 times larger

Table 3. Optical geometries (in units of mm).

α	L_0	L_1	L'_m	L_3	L_{tot}	L_{full}
1	394 ± 2	788 ± 2	264 ± 0.5	788 ± 2	1840 ± 2	2234 ± 2
5	761 ± 2	415 ± 10	264 ± 0.5	2678 ± 2	3357 ± 10	4418 ± 10
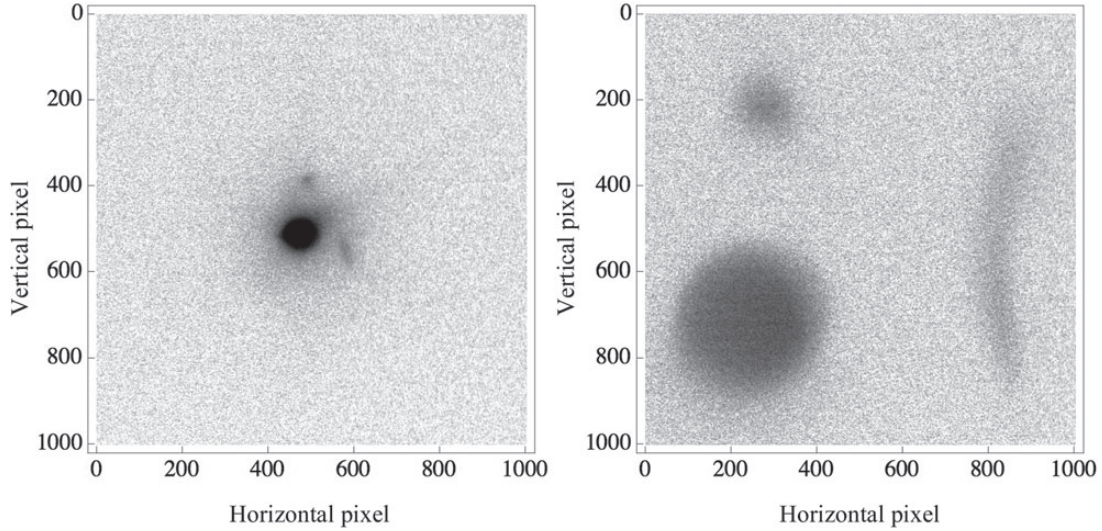
Fig. 15. Images of the sample mask obtained with the optical arrangements for (left) $\alpha = 1$ and (right) $\alpha = 5$, where the contrast was calibrated by each measurement time and plotted from minimum to maximum values of each image on a log scale. Both frames indicate $50\,\text{mm} \times 50\,\text{mm}$ in real space.

than that for $\alpha = 1$. The two images for both $\alpha = 1$ and 5 showed some distortion, which may have been caused by the misalignment of the mask, lens, and NIP, and contamination with higher-order magnetic fields. Note that α is rather sensitive to the distance between the mask and the lens in the case of such a large magnification. In addition, since the NIP detects all the neutrons regardless of the TOF, neutrons with wavelengths outside the manageable wavelength range also contaminate the image. These effects may have also caused the observed discrepancy of the magnification factor α. The effects of such aberrations should be the subject of future studies.

4. Conclusions and perspectives

The triplet mod-PMSx proposed in this study exhibited excellent focusing performance for a pulsed neutron beam over the wavelength range of λ_{min}–$2\lambda_{min}$, which is wide for a magnetic lens, while the effect of chromatic aberration on the beam spot size was sufficiently suppressed for the focused beam to remain the same size as the source aperture. A VCN beam with wavelengths in the range of 27–55 Å was focused to the size of the source aperture of 2 mm diameter in a total focusing distance of 1.84 m. The average gain in beam flux of the focused beam relative to the polarized unfocused beam was 43 in the wavelength range.

The demonstration of neutron image magnification produced an image with a magnification of 4.1 at the detection point. This proves the feasibility of the mod-PMSx for high-resolution imaging. Furthermore, it has been proven that large and off-axis sources can be focused and magnified by a mod-PMSx lens.

The mod-PMSx lens consisted of three lens units, and its cascaded modular structure successfully demonstrated the wide applicability of mod-PMSx lens devices for various instrument requirements. In principle, the achieved wavelength range of the mod-PMSx of $\kappa_\lambda = \lambda_{max}/\lambda_{min} = 2$ holds for any neutron energy range. In the case of a cold neutron beam with a wavelength from 5 to 10 Å, a mod-PMSx with an effective magnet length of 2 m, which consists of 30 cascaded units, can focus the beam in a reasonable total focusing distance of 6.5 m. Calculation results for the magnetic field show that κ_λ of the mod-PMSx can also exceed 5 by adjusting the pole size in the extended-Halbach-type sextupole magnet. Then, for instance, a cold neutron beam with a wavelength from 3 to 15 Å could be focused.

The mod-PMSx is a simple system consisting of permanent magnets and controllable generic motors. It does not require any large subsidiary equipment or facilities such as a cryostat or a bulky power supply, or any special techniques for its construction or operation. Furthermore, the magnetic torque canceler contributes to making the mod-PMSx compact and light. Therefore, it can be widely used in TOF-type instruments worldwide.

Appendix

The solutions to Eq. (3) are given by the following 6D transfer matrix in phase space:

$$
\begin{pmatrix} x \\ v_x \\ y \\ v_y \\ z \\ v_z \end{pmatrix} = \begin{pmatrix} \cos(\omega t) & \omega^{-1}\sin(\omega t) & 0 & 0 & 0 & 0 \\ -\omega\sin(\omega t) & \cos(\omega t) & 0 & 0 & 0 & 0 \\ 0 & 0 & \cos(\omega t) & \omega^{-1}\sin(\omega t) & 0 & 0 \\ 0 & 0 & -\omega\sin(\omega t) & \cos(\omega t) & 0 & 0 \\ 0 & 0 & 0 & 0 & 1 & t \\ 0 & 0 & 0 & 0 & 0 & 1 \end{pmatrix} \begin{pmatrix} x_i \\ v_{xi} \\ y_i \\ v_{yi} \\ z_i \\ v_{zi} \end{pmatrix}, \quad (A1)
$$

where the subscript i indicates the initial state. Since the motion of a neutron along each axis is independent, the propagation on the transverse plane can be expressed in the following shortened form:

$$
\begin{pmatrix} x(t) & y(t) \\ v_x(t) & v_y(t) \end{pmatrix} = \mathbf{M} \begin{pmatrix} x_i & y_i \\ v_{xi} & v_{yi} \end{pmatrix}, \quad (A2)
$$

$$
\mathbf{M} = \begin{cases} \mathbf{M}_P = \begin{pmatrix} \cos(\omega t) & \omega^{-1}\sin(\omega t) \\ -\omega\sin(\omega t) & \cos(\omega t) \end{pmatrix} & \text{parallel spin} \\[2em] \mathbf{M}_A = \begin{pmatrix} \cosh(\omega t) & \omega^{-1}\sinh(\omega t) \\ \omega\sinh(\omega t) & \cosh(\omega t) \end{pmatrix} & \text{antiparallel spin} \end{cases}, \quad (A3)
$$

where $v_x = dx/dt$ and $v_y = dy/dt$ are the transverse velocities. By scaling the transverse velocities by ω, $\xi = v_x/\omega$, and $\eta = v_y/\omega$, Eqs. (A2) and (A3) are rewritten as

$$\begin{pmatrix} x(t) & y(t) \\ \xi(t) & \eta(t) \end{pmatrix} = \mathbf{M} \begin{pmatrix} x_i & y_i \\ \xi_i & \eta_i \end{pmatrix}, \tag{A4}$$

$$\mathbf{M} = \begin{cases} \mathbf{M}_P = \begin{pmatrix} \cos(\omega t) & \sin(\omega t) \\ -\sin(\omega t) & \cos(\omega t) \end{pmatrix} & \text{parallel spin} \\[2mm] \mathbf{M}_A = \begin{pmatrix} \cosh(\omega t) & \sinh(\omega t) \\ \sinh(\omega t) & \cosh(\omega t) \end{pmatrix} & \text{antiparallel spin} \end{cases} . \tag{A5}$$

Neutrons with a parallel spin oscillate along the beam axis, while those with an antiparallel spin diverge. The sextupole field $\mathbf{B}_6$ can act as a focusing lens for neutrons with parallel spins, which increases the beam flux at the image plane. Since diverging neutrons with an antiparallel spin would cause background noise, the beam is usually polarized parallel to the magnetic field in advance by installing a polarizer upstream. The effect of focusing on a parallel-spin neutron is isotropic because the equations of motion (Eq. (3)) are symmetric on the xy-plane.

Using the same notation as in Eqs. (A4) and (A5), the transfer matrix in the drift space shown in Fig. 1 is given by

$$\mathbf{M}_0 = \begin{pmatrix} 1 & \omega t \\ 0 & 1 \end{pmatrix}. \tag{A6}$$

Since the equations of vertical and horizontal motion on the xy-plane are symmetric provided gravity is neglected, we only discuss the variable x. The phase space coordinates at P_3 in Fig. 1 are given by

$$\mathbf{X}_3 = \begin{pmatrix} x_3 \\ \xi_3 \end{pmatrix} = \mathbf{M}_3 \mathbf{M}_2 \mathbf{M}_1 \mathbf{X}_0 = \begin{pmatrix} 1 & \omega t_{32} \\ 0 & 1 \end{pmatrix} \begin{pmatrix} \cos(\omega t_{21}) & \sin(\omega t_{21}) \\ -\sin(\omega t_{21}) & \cos(\omega t_{21}) \end{pmatrix} \begin{pmatrix} 1 & \omega t_{10} \\ 0 & 1 \end{pmatrix} \begin{pmatrix} x_0 \\ \xi_0 \end{pmatrix}$$

$$= \begin{pmatrix} x_0\{\cos(\omega t_{21}) - \omega t_{32}\sin(\omega t_{21})\} + \xi_0\{\omega(t_{10} + t_{32})\cos(\omega t_{21}) + (1 - \omega t_{10}\omega t_{32})\sin t(\omega t_{21})\} \\ -x_0\sin(\omega t_{21}) - \xi_0(\omega t_{10}\sin(\omega t_{21}) - \cos(\omega t_{21})) \end{pmatrix}, \tag{A7}$$

where the subscripts $j = 0, 1, 2$, and 3 indicate P_0, P_1, P_2, and P_3, respectively. The flight times between these points are denoted as $t_{10} = t_1 - t_0$, $t_{21} = t_2 - t_1$, and $t_{32} = t_3 - t_2$. When the neutron beam forms an image at P_3, x_3 should be independent of ξ_0. Therefore, the focusing condition is derived as

$$\begin{cases} \cos(\omega t_{21}) = \dfrac{\omega t_{10}\omega t_{32} - 1}{\omega t_{10} + \omega t_{32}} & (0 < \omega t_{21} < \pi) \\[3mm] t_{10} = t_{32} = 0 & (\omega t_{21} = \pi) \end{cases} . \tag{A8}$$

As mentioned in Sect. 2.1.1, we assume that the transverse velocities of a neutron, v_x and v_y, are so small compared with v_z that the neutron velocity v can be approximated by the velocity along the beam axis $v_z : v \sim v_z$. In accordance with the TOF method, the neutron velocity v_z and wavelength

λ of a pulsed beam are obtained from the time of flight t and path length L as follows:

$$v_z = \frac{L}{t} = \frac{h}{M\lambda},\tag{A9}$$

where h and M are Planck's constant and the mass of a neutron, respectively. Here, introducing the new parameter

$$\Omega \equiv \omega/v_z,\tag{A10}$$

the phase ωt is converted into ΩL. The transfer matrix Eq. (A6) and the focusing condition Eq. (A7) can be expressed as functions of L:

$$\mathbf{X}_3 = \mathbf{M}_3\mathbf{M}_2\mathbf{M}_1\mathbf{X}_0 = \begin{pmatrix} 1 & \Omega \cdot L_3 \\ 0 & 1 \end{pmatrix} \begin{pmatrix} \cos(\Omega \cdot L_m) & \sin(\Omega \cdot L_m) \\ -\sin(\Omega \cdot L_m) & \cos(\Omega \cdot L_m) \end{pmatrix} \begin{pmatrix} 1 & \Omega \cdot L_1 \\ 0 & 1 \end{pmatrix} \begin{pmatrix} x_0 \\ \xi_0 \end{pmatrix},\tag{A11}$$

$$\begin{cases} \cot(\Omega \cdot L_{\mathrm{m}}) = \dfrac{\Omega(L_1 L_3 - 1/\Omega^2)}{L_1 + L_3} & (0 < \Omega \cdot L_{\mathrm{m}} < \pi) \\[2mm] L_1 = L_3 = 0 & (\Omega \cdot L_{\mathrm{m}} = \pi) \end{cases}.\tag{A12}$$

Equation (A11) gives conditions on L_{m}, L_1, and L_3 in Fig. 1 so that the beam is focused at P$_3$.

References

[1] P. Mikula et al., J. Appl. Crystallogr. **19**, 324 (1986).
[2] M. R. Eskildsen et al., Nature **391**, 563 (1998).
[3] S. M. Choi et al., J. Appl. Crystallogr. **33**, 793 (2000).
[4] B. E. Allman, A. Cimmino, and S. L. Griffin, Neutron News **10**, 20 (1999).
[5] B. Alefeld et al., Physica B **234-236**, 10522 (1997).
[6] D. F. Mildner and M. V. Gubarev, Nucl. Instrum. Meth. A **634**, 7 (2011).
[7] P. S. Farago, Nucl. Instrum. Methods **30**, 271 (1964).
[8] H. M. Shimizu et al., Nucl. Instrum. Meth. A **430**, 423 (1999).
[9] T. Oku et al., Physica B **385-386**, 1225 (2006).
[10] S. Koizumi et al., J. Appl. Crystallogr. **40**, 474 (2007).
[11] NG7 SANS at NIST, (Available at: http://www.nist.gov/ncnr/ng7sans.cfm, date last accessed 20 December 2014).
[12] E. P. Gilbert et al., Physica B **385-386**, 1180 (2006).
[13] J. Suzuki et al., Nucl. Instrum. Meth. A **529**, 120 (2004).
[14] T. Oku et al., Appl. Phys. A **74** [Suppl.], S261 (2002).
[15] T. Oku et al., Nucl. Instrum. Meth. A **600**, 100 (2009).
[16] T. Oku et al., J. Phys.: Conf. Ser. **251**, 012078 (2010).
[17] Y. Iwashita et al., Nucl. Instrum. Meth. A **586**, 73 (2008).
[18] Y. Iwashita et al., IEEE Trans. Appl. Supercond. **20**, 842 (2010).
[19] M. Yamada et al., Physica B **404**, 2646 (2009).
[20] B. Alefeld et al., Physica B **283**, 330 (2000).
[21] E. Kentzinger et al., Physica B **350**, 779 (2004).
[22] D. Liu et al., Nature Commun. **4**, 2556 (2013).
[23] G. E. Ice et al., Mater. Sci. Eng. A **437**, 120 (2007).
[24] T. Shinohara et al., Nucl. Instrum. Meth. A **600**, 111 (2009).
[25] T. Shinohara et al., XIV International Conference on Small-Angle-Scattering (SAS2009), Oxford, UK, September 2009.
[26] H. Iwashita et al., Nucl. Instrum. Meth. A **600**, 129 (2009).
[27] J. Suzuki et al., J. Appl. Crystallogr. **36**, 795 (2003).
[28] H. M. Shimizu et al., Nucl. Instrum. Meth. A **529**, 5 (2004).
[29] T. Oku et al., Nucl. Instrum. Meth. A **529**, 116 (2004).

[30] T. Oku et al., Physica B **356**, 126 (2005).
[31] M. Yamada et al., Nucl. Instrum. Meth. A **634**, S156 (2011).
[32] M. Yamada, Physica B **406**, 2453 (2011).
[33] M. Yamada, *Ph.D. Thesis*, Kyoto University (2013) [in Japanese].
[34] Y. Iwashita et al., IEEE Trans. Appl. Supercond. **22**, 4000905 (2012).
[35] M. Kumada et al., IEEE Trans. Appl. Supercond. **12**, 129 (2002).
[36] M. Kumada et al., IEEE Trans. Appl. Supercond. **14**, 1287 (2004).
[37] K. Halbach, Nucl. Instrum. Meth. A **169**, 1 (1980).
[38] Y. Iwashita et al., Nucl. Instrum. Meth. A **586**, 73 (2008).
[39] Y. Iwashita et al., IEEE Trans. Appl. Supercond. **18**, 957 (2008).
[40] E. I. du Pont de Nemours and Company, (Available at: http://www.dupont.com/products-and-services/fabrics-fibers-nonwovens/fibers/brands/kevlar.html, date last accessed 20 December 2014).
[41] T. Oku et al., J. Appl. Crystallogr. **40**, 408 (2007).
[42] ILL PF2 group, (Available at: http://www.ill.eu/instruments-support/instruments-groups/instruments/pf2/characteristics/, date last accessed 20 December 2014).
[43] M. Hino et al., Physica B **385-386**, 1187 (2006).
[44] M. James et al., Nucl. Instrum. Meth. A **632**, 112 (2011).
[45] K. Hirota et al., Phys. Chem. Chem. Phys. **7**, 1836 (2005).
[46] A. Steyerl et al., Phys. Lett. A **116**, 347 (1986).